SOLID FREEFORM FABRICATION 2021

Microstructure and Deformation Behavior of Additively Manufactured 17–4 Stainless Steel: Laser Powder Bed Fusion vs. Laser Powder Directed Energy Deposition

P.D. NEZHADFAR,[1,2] PAUL R. GRADL,[3] SHUAI SHAO,[1,2] and NIMA SHAMSAEI [1,2,4]

1.—Department of Mechanical Engineering, Auburn University, Auburn, AL 36849, USA. 2.—National Center for Additive Manufacturing Excellence (NCAME), Auburn University, Auburn, AL 36849, USA. 3.—Propulsion Department, NASA Marshall Space Flight Center, Huntsville, AL 35812, USA. 4.—e-mail: shamsaei@auburn.edu

This study aims to compare the microstructure of 17–4 PH stainless steel (SS) manufactured via laser powder bed fusion (L-PBF) and laser powder directed energy deposition (LP-DED) in non-heat treated (NHT) and heat treated conditions. In addition, the room-temperature tensile behavior of heat-treated L-PBF and LP-DED 17–4 PH SS has been investigated and compared with that of the wrought counterpart with the same heat treatment conditions. The results show that the L-PBF specimens have a finer microstructure (ferrite + lath martensite) than the LP-DED ones (massive ferrite + Widmanstätten ferrite) in NHT condition. Electron backscatter diffraction analysis shows that the L-PBF and LP-DED specimens have twin-based substructure lath martensite after heat treatment. Despite the lower tensile strength of the LP-DED specimens compared with the L-PBF ones, the ductility of peak-aged LP-DED specimens was reduced due to the presence of the δ-ferrite phase having a significant plastic deformation incompatibility with the martensite.

INTRODUCTION

Additive manufacturing (AM) has transformed the manufacturing process of structural parts in various industries such as aerospace, automotive, biomedical, defense, and nuclear. The layer-by-layer and track-by-track nature of AM processes allows the manufacture of near-net-shaped parts with complex geometries, reduces the cost and lead times, and facilitates the fabrication of highly customized parts for specific applications (e.g., in the medical field).[1] There are various types of AM techniques for metallic materials classified based on feedstock form (e.g., powder versus wire), feeding mechanism (e.g., powder bed versus blown powder), and energy source (e.g., laser versus electron beam).[2]

Among the various AM processes, laser powder bed fusion (L-PBF) and laser powder directed energy deposition (LP-DED) are the most prominent laser-based processes, which have been extensively investigated in the literature.[3] The L-PBF process provides more freedom in designing near-net-shaped parts with higher geometrical resolution and precision than the LP-DED process; however, L-PBF is typically limited to a single-powder feedstock.[4] On the other hand, LP-DED offers better compatibility for multi-powder feedstock, functionally graded components, and the fabrication of large parts.[1]

One of the specific characteristics of the laser-based AM processes is the high heating/cooling rates during fabrication, resulting in a refined microstructure compared to conventionally manufactured (CM) counterparts. Accordingly, the AM materials often have static mechanical properties comparable to, and in some cases outperforming, their CM counterparts.[5,6] The mechanical performance of the AM materials is primarily influenced

by the material's structure (i.e., grain structure, texture, surface roughness, and defect structure), which is impacted by the thermal history induced during the manufacturing. The thermal history itself is governed by the process parameters (i.e., powder, scan speed, etc.) and design parameters (i.e., part size and geometry, time interval, etc.). In addition to the above-mentioned influential parameters, the AM process technique (e.g., L-PBF, LP-DED, etc.) itself may also cause variations in the microstructural and mechanical properties of a material system.

The LP-DED process, due to the slower moving melt pool (typically ~10–30 mm/s[7] compared to ~1000–1700 mm/s for L-PBF[8]) created by a high powered laser (typically ~1000 W), has a considerably lower cooling rate (by approximately three orders of magnitude) than L-PBF,[9,10] giving the fabricated materials a distinct microstructure (i.e., grain structure, crystallographic texture, precipitations, etc.) and defect content. Amato et al.[11] reported the presence of a spheroidal/ellipsoidal γ" in γ matrix of non-heat treated (NHT) L-PBF IN718, while Laves phase has been characterized in an interdendritic γ matrix of NHT LP-DED counterparts[12,13] Xu et al.[14] reported a lamellar α+ß structure in L-PBF Ti-6Al-4V, whereas Caroll et al.[15] showed a Widmanstätten structure along with grain boundary α phase in the coarse columnar prior β grains in LP-DED Ti-6Al-4V. It has been reported that even post-thermal heat treatment may not completely diminish the differences in the microstructure of the L-PBF and LP-DED AM materials. Schneider et al.[16] reported different grain structures (i.e., size and morphology) for L-PBF and LP-DED IN718 even after applying a similar heat treatment procedure, which was attributed to the variation in their initial microstructure (i.e., NHT condition). The L-PBF specimens showed the highest degree of homogenization and more refined grains than the LP-DED ones.

The microstructure variations of the L-PBF and LP-DED AM materials result in different mechanical responses. Babuska et al.[4] recently reported a higher tensile strength for L-PBF CoCr specimens than for LP-DED counterparts. They attributed this to the finer microstructure of the L-PBF specimens due to the higher cooling rate compared with the LP-DED ones. Donate-Buendia et al.[17] compared the microstructure, and mechanical properties of oxide dispersion strengthened (ODS) steels manufactured via L-PBF and LP-DED processes. Compared to LP-DED, the L-PBF process produced a finer grain structure, reduced the agglomeration of the strengthening particles (i.e., Y_2O_3), and yielded higher hardness values in the ODS steel.

The significant dependence of the microstructure and mechanical properties of such known materials as IN718, Ti-6Al-4V, ODS steels, etc. on AM processes necessitates the careful evaluation of this dependence before mass adoption of AM to any other materials in key industrial sectors. The 17-4 precipitation hardening (PH) stainless steel (SS) is one of the most commonly used materials in various industries (e.g., aerospace, energy, food processing, etc.) due to its favorable chemical and mechanical properties (e.g., high corrosion resistance, high strength, and ductility, etc.).[18] It has recently drawn much attention from the AM community due to its superior weldability.[19,20] The sensitivity of its microstructure to the cooling rate during solidification, as well as the subsequent thermal exposures, can potentially make the properties of 17–4 PH SS process-dependent. This study investigates and compares the microstructure and room-temperature tensile behavior of 17–4 PH SS manufactured by the L-PBF and LP-DED processes. The grain structure and phase constituent of the L-PBF and LP-DED 17–4 PH SS specimens are characterized and compared in the NHT condition. In addition, the effect of various heat treatment conditions on the crystallographic texture and room-temperature tensile behavior of the L-PBF and LP-DED 17–4 PH SS specimens is investigated.

EXPERIMENTAL

Two batches of argon-atomized 17–4 PH SS powder were used to fabricate the specimens via the L-PBF and LP-DED processes, respectively. The detailed chemical compositions of the 17–4 PH SS powders used for each AM process are listed in Table I.

An EOS M290 machine was used to fabricate the L-PBF cylindrical bars (ϕ11 mm). The EOS default process parameters, laser power of 220 W, scan speed of 755 mm/s, hatching distance of 0.1 mm, and layer thickness of 0.04 mm, were employed, and nitrogen was used as the shielding gas. The LP-DED cylindrical bars (ϕ15.24 mm) were fabricated using an RPM Innovations (RPMI) 557 machine. The process parameters were: power of 1070 W, layer height of 0.38 mm, travel speed of 1,016 mm/min, and powder feed rate of 15.1 g/min, with argon used as the shielding gas.

Table I. Chemical composition of 17-4 PH SS powders used for fabrication

		C	Cr	Ni	Cu	Mn	Si	Nb	Mo	N	O	P	S	Nb+Ta	Fe
L-PBF	(Wt.%)	0.01	15.80	4.60	3.67	0.51	0.32	0.32	0.21	0.02	0.04	0.035	0.014	0.27	Bal.
LP-DED	(Wt.%)	0.01	16.39	4.17	3.32	0.06	0.78	0.27	0.04	0.01	0.02	0.00	0.00	0.27	Bal.

Microstructure and Deformation Behavior of Additively Manufactured 17–4 Stainless Steel:
Laser Powder Bed Fusion vs. Laser Powder Directed Energy Deposition

The Thermo-Calc. software was used to generate the Fe-Cr binary phase diagram to analyze the phase transformations possible for 17-4 PH SS. The TCFE9 thermodynamic database for various Fe-based alloys and steels such as stainless steels was employed.[21,22] In addition, to incorporate the influence of all the alloy elements in generating the phase diagram, the Ni_{eq} (nickel equivalent) and Cr_{eq} (chromium equivalent) were obtained following the Schaeffler equations:[23]

$$Ni_{eq}(wt\%) = \%Ni + 0.5(\%Mn) + 0.3(\%Cu) + 25(\%N) + 30(\%C) \tag{1}$$

$$Cr_{eq}(wt\%) = \%Cr + 2(\%Si) + 1.5(\%Mo) + 1.75(\%Nb) \tag{2}$$

The Ni_{eq} and Cr_{eq} values were further calculated for the L-PBF to be 7.6 wt% and 16.6 wt%, respectively. For the LP-DED 17-4 PH SS, the Ni_{eq} and Cr_{eq} values were 6.1 and 17.7 wt%, respectively. Figure 1 shows the binary phase diagram generated by Thermo-Calc. software; the Cr amounts for the L-PBF and LP-DED specimens are indicated on the phase diagram to predict the phase constituents at various temperatures. According to the phase diagram, the stress relieve (SR) heat treatment was carried out at 650°C/1 h for the L-PBF and LP-DED specimens. It has been reported in Ref. 24 that this SR procedure changes neither the microstructure nor the mechanical properties of the L-PBF and LP-DED 17-4 PH SS. All the L-PBF and LP-DED specimens underwent hot isostatic pressing (HIP) at 1163°C/3 h under 103 MPa pressure and were solution (Sol) treated at 1050°C/0.5 h [i.e., Condition A (CA)] followed by air cooling. Some specimens for each type (i.e., L-PBF and LP-DED specimens) were aged at 482°C/1 h (i.e., H900) known as peak-age, and some were over-aged at 621°C/4 h (i.e., H1150). In the following text, the heat-treated specimens (i.e., SR + HIP + Sol + Age) are dubbed CA-H900 and CA-H1150. After the full heat treatment, all the specimens were machined to the final tensile testing geometry following the ASTM E8 standard.[25]

The L-PBF and LP-DED specimens were cut in the gage section transversely parallel to the build direction for microstructure characterization prior to tensile testing. The microstructure was characterized in NHT and fully heat treated conditions. The samples were ground and polished using sandpapers with grits 320–4000 followed by a mirror-finish polishing step using Chemo-met along with a 0.2-μm colloidal silica suspension. The microstructure was further characterized on the plane parallel (XZ-plane) to the build direction using a Zeiss Crossbeam 550 scanning electron microscope (SEM) with an electron backscatter diffraction (EBSD) detector. The specimens were mirror-finished using a vibratory polisher for 2 h before conducting the EBSD analysis and electron channeling contrast imaging (ECCI).
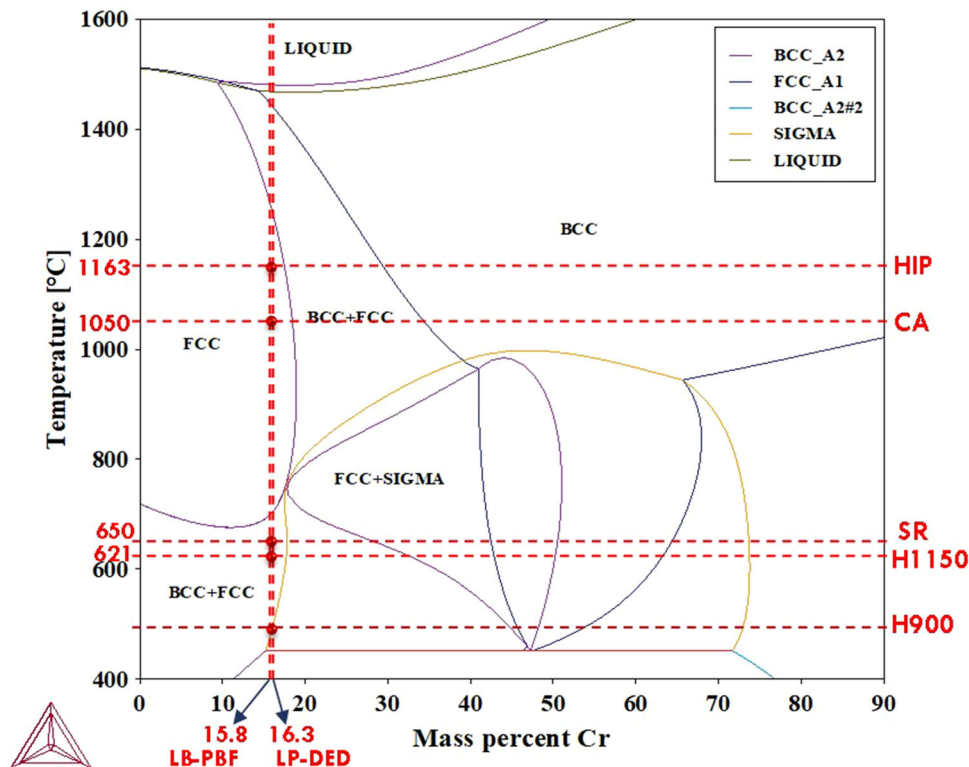

Fig. 1. Ni-Cr binary phase diagram samples generated by Thermo-Calc. software using the TCFE9 thermodynamic database[22].

The tensile tests were conducted on the heat-treated L-PBF and LP-DED 17-4 PH SS specimens at room temperature at 0.005 mm/mm/min strain rate. The fracture surfaces were further cleaned in a bath of isopropanol and water using an ultrasonic cleaner before performing fractography using SEM.

RESULTS AND DISCUSSION

NHT Microstructure

The NHT microstructures of the L-PBF and LP-DED 17-4 PH SS specimens characterized via EBSD analysis and ECCI are shown in Fig. 2. It is evident that the L-PBF 17-4 PH SS specimen (Fig. 2a) has a more refined grain structure as compared to the LP-DED 17–4 PH SS one (Fig. 2b); the L-PBF specimen consists of fine, primarily equiaxed, ferrite grains, whereas the LP-DED one consists of very coarse columnar ferrite grains. The ECCI images with higher magnifications reveal that the microstructure of the L-PBF specimen consists of ferrite and lath martensite. In contrast, the LP-DED specimen has a ferritic microstructure consisting of massive ferrite grains with Widmanstätten ferrites decorating the grain boundaries.

Since the martensite start temperature (i.e., M_s) is above room temperature for the 17–4 PH SS (M_s = 100–150°C),[26,27] the austenite formed during solidification transforms to the martensite upon cooling to room temperature. However, the ferritic microstructure of the NHT AM 17-4 PH SS specimens, regardless of the manufacturing technique, has been attributed to the "austenite by-passing" mechanism. In this mechanism, the ferrite phase formed from the liquid will not transfer to the austenite due to the high cooling rate in AM processes as compared to conventional manufacturing techniques (e.g., casting, forging, etc.).[28]

The lath martensite in the microstructure of L-PBF 17-4 PH SS specimen (see Fig. 2a), however, indicates that the austenite has been formed during the solidification. This may be attributed to the N_2 shielding gas used to fabricate the L-PBF specimens. It has been reported that N_2 as the shielding gas refines the grain structure and also stimulates austenite formation during solidification.[20,29,30] Therefore, the refined ferrite grains (average grain size of ~6 μm) and the lath martensite in the microstructure are the result of using N_2 as shielding gas. The coarse microstructure of the LP-DED
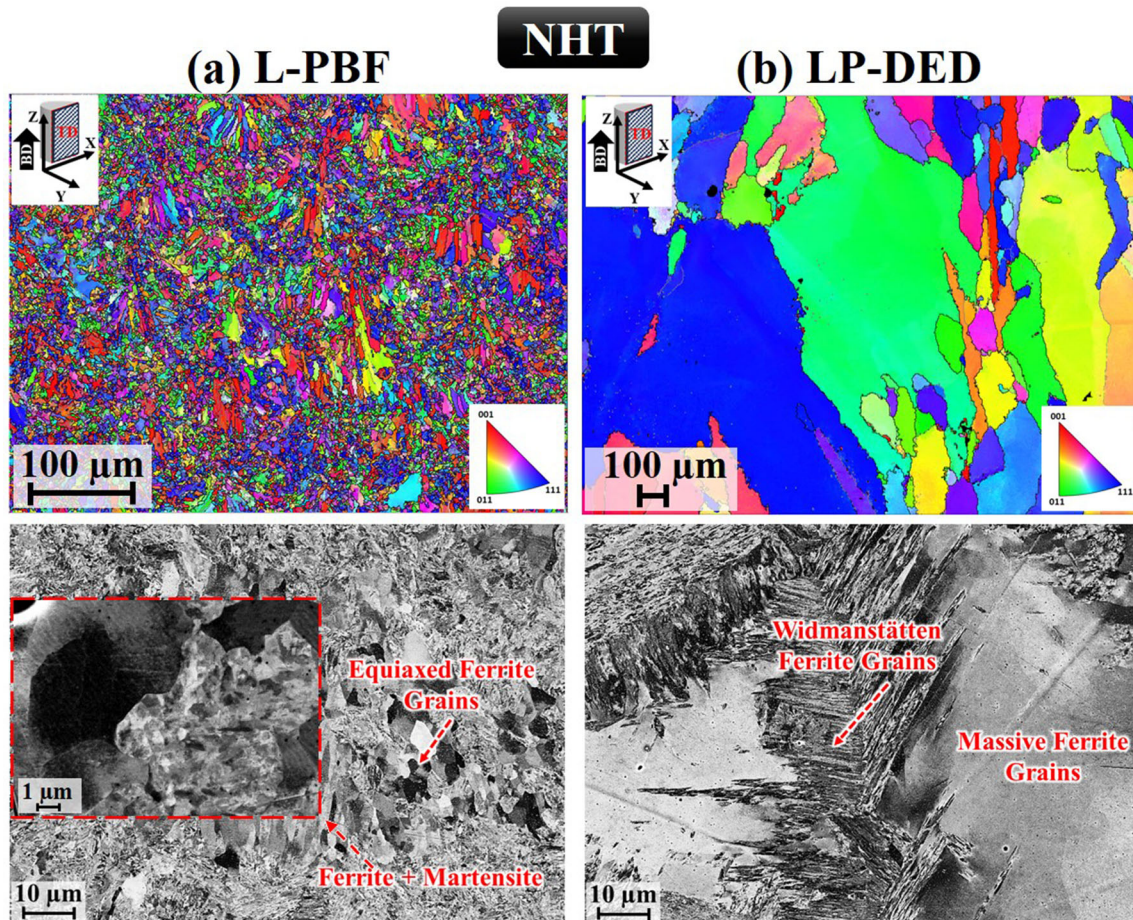

Fig. 2. Inverse pole figure (IPF) maps along the Z direction and ECCI micrographs of (a) L-PBF, and (b) LP-DED 17-4 PH SS specimens in NHT condition.

17-4 PH SS specimen (average grain size of ∼93.1 μm) may be attributed to the lower cooling rate induced in the LP-DED process as compared to the L-PBF one. Although the cooling rate of the LP-DED process is believed to be above the threshold for austenite by-passing, it has been reported to have almost a two to three orders of magnitude slower cooling rate than the L-PBF process.[4] In addition, the ferrite phase is more stabilized in LP-DED specimens due to the higher Cr_{eq}/Ni_{eq} value for the LP-DED 17-4 PH SS (∼2.9) compared to that of the L-PBF counterpart (∼2.1). The significantly different NHT microstructures of the L-PBF and LP-DED 17-4 PH SS specimens may not only lead to drastically different mechanical properties but also may be inferior in strength due to the absence of precipitates. In hope to resolve these issues, post-thermal treatments are typically performed to enhance the mechanical properties of the material, as well as reducing the differences in the microstructures of the L-PBF and LP-DED specimens.

Heat Treated Microstructure

The microstructure of the L-PBF and LP-DED 17-4 PH SS specimens are compared in Fig. 3 for the CA-H900 and CA-H1150 heat treatment conditions. Although there is a visible difference between the microstructures of the NHT L-PBF and LP-DED 17-4 PH SS specimens (see Fig. 2), post-thermal treatment (i.e., SR + HIP + HT) have evidently altered the microstructures to martensite-dominated ones for both the L-PBF and LP-DED specimens (see Fig. 3). It can be seen in Fig. 3a and c that both the L-PBF and LP-DED have a primarily martensitic microstructure in the CA-H900 heat treatment condition with a minimal fraction of retained austenite (∼0.1%). The fraction of retained austenite is increased for both the L-PBF (Fig. 3b) and LP-DED (Fig. 3d) specimens that have undergone CA-H1150 heat treatment. This is due to the diffusion of austenite stabilizer elements (i.e., Cu, Ni, N, etc.) to the grain boundaries during the long-term aging (i.e., 4 h) at a temperature close to the austenite reversion (see Fig. 1), which may have resulted in the nucleation of austenite grains.[31] However, depending on the size of the reverted austenite grains, they may or may not transform to
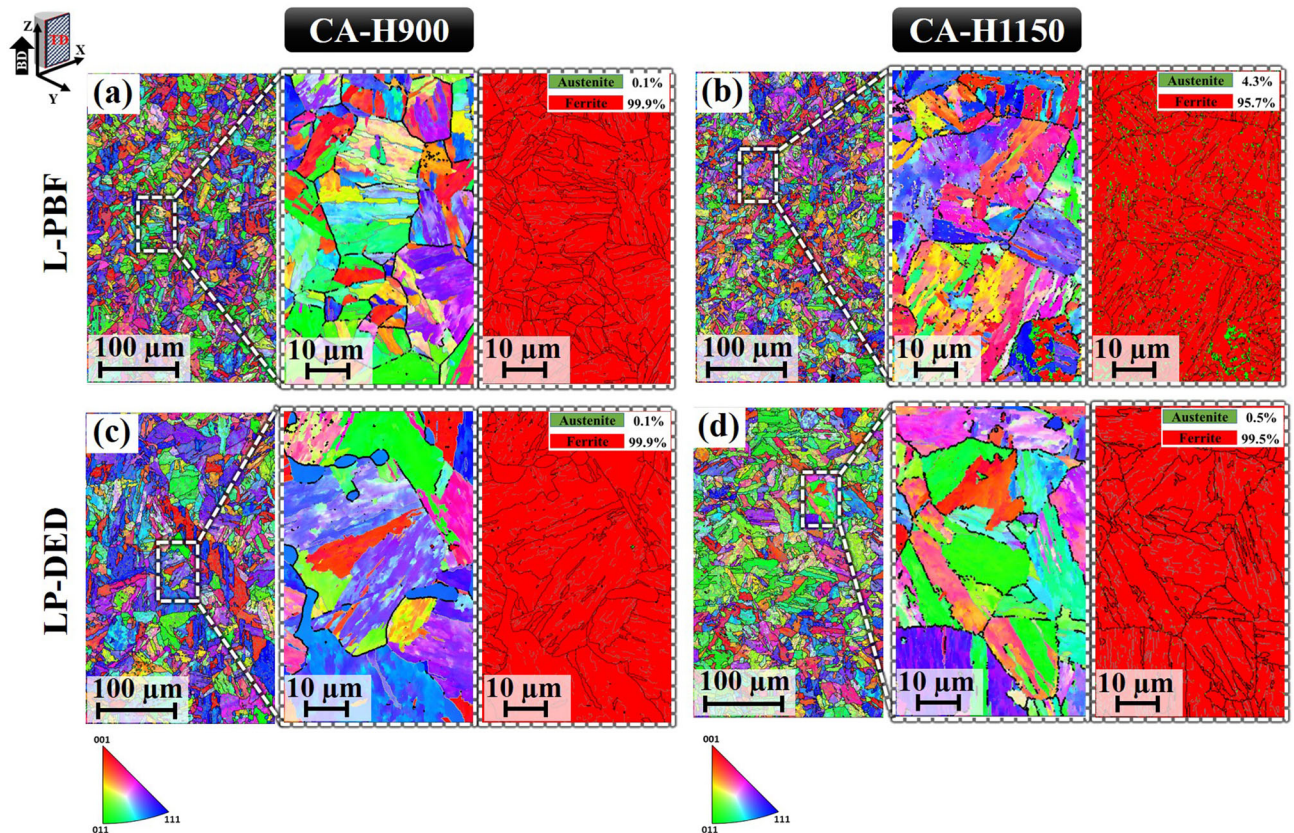

Fig. 3. IPF maps (along the Z direction) and phase maps for the heat treated 17-4 PH SS specimens: (a) L-PBF and (c) LP-DED at CA-H900, and (b) L-PBF and (d) LP-DED at CA-H1150. Note that the black boundaries in the magnified IPF maps (in the middle) represent the prior austenite grain boundaries.

martensite upon cooling. It has been well established that martensitic transformations are more difficult for finer austenite grains, which may be retained after heat treatment.[32]

As seen in Fig. 3b for the CA-H1150-treated L-PBF specimen, the fraction of austenite ($\sim$4.3%) retained in the microstructure is higher than that of the CA-H1150 LP-DED counterpart ($\sim$0.5%), shown in Fig. 3d. This can be partially ascribed to the finer initial microstructure of the L-PBF specimen compared with that of the LP-DED one, which results in finer reverted austenite grains that are more difficult to transform to martensite upon cooling. Moreover, using N_2 shielding gas for fabrication may increase the austenite stabilization and hinder the martensitic transformation. It can be observed that the δ-ferrite phase is retained in the microstructure of the LP-DED specimens (see Fig. 3c and d), regardless of the heat treatment condition, whereas the δ-ferrite phase is absent in the microstructure of the N_2-shielded L-PBF specimens. The N_2 shielding gas has been reported to reduce the δ-ferrite phase fraction retained in the microstructure of laser-welded materials at room temperature. N as an austenite stabilizer results in the transformation of the δ-ferrite phase to austenite during the solidification, which reduces the fraction of δ-ferrite phase retained in the microstructure at room temperature. Moreover, the L-PBF specimen has a lower Cr_{eq}/Ni_{eq} value than the LP-DED one, reducing ferrite stability during solidification.

Texture Analysis

The variation in thermal history induced via L-PBF and LP-DED processes influences the crystallographic texture of the AM 17–4 PH SS specimens. It has been shown that the NHT L-PBF 17–4 PH SS specimen possesses a strong cube along with weak γ-fiber texture components, whereas no specific texture component has been reported for the NHT LP-DED 17-4 PH SS specimen due to its very large grain structure (see Fig. 2b).[24] In addition, it has been reported that performing SR heat treatment assists with the recrystallization upon further heat-treatment procedures and weakens the texture.[24] To understand and compare the crystallographic textures of the L-PBF and LP-DED 17–4 PH SS specimens after applying full heat treatments (i.e., SR + HIP + Sol + Age), their corresponding orientation distribution function (ODF) maps for each condition are presented in Figs. 4 and 5. The ODF maps have been analyzed in parallel to the build and loading direction (i.e., Z) using a spherical harmonics method, keeping the Euler angle 3 (i.e., φ_2) constant. The quantified fraction of the essential texture components, i.e., Cube (C), Rotated Cube (RC), Copper (Cu), Transformed Copper (TC), Goss (G), Transformed Goss (TG), Brass (B), Transformed Brass (TB), and γ-fiber) are presented and

compared for the L-PBF and LP-DED specimens in both CA-H900 and CA-H1150 conditions.

In addition to the ODF maps ($0 \leq \Phi_1$, Φ, $\varphi_2 \leq 90$), the fraction of texture components for the L-PBF and LP-DED specimens which have undergone CA-H900 and CA-H1150 heat treatments are also provided in Figs. 4c and 5c, respectively. In the CA-H900 heat treatment condition, the L-PBF specimen (see Fig. 4a) has a lower texture intensity [i.e., multiple random density (mrd)], $mrd_{max} = 1.85$, than the LP-DED one, $mrd_{max} = 3.25$ (see Fig. 4b). This is likely due to the finer grain structure of the L-PBF specimen and most likely with more randomly oriented grains than LP-DED one. The texture intensities for both the L-PBF and LP-DED specimens are reduced as compared to their NHT conditions ($(mrd_{max})_{L-PBF} = 2.03$, $(mrd_{max})_{LP-DED} = 20.87$) reported in[24] and become more randomized. This is ascribed to the recrystallization occurring during HIP and to further heat treatment procedures (i.e., Sol + Age). Therefore, full heat treatment could to some extent weaken texture differences between the L-PBF and LP-DED 17–4 PH SS specimens induced due to the differences in the cooling rates of the AM processes.

The main texture component for the L-PBF specimen at the CA-H900 heat treatment condition is TB, whereas TC1 is the main texture component for the LP-DED specimen (see Fig. 4c). It can be seen in Fig. 5c that the conducting CA-H1150 heat treatment will result in a more similar trend of texture component fractions in the L-PBF and LP-DED specimens as compared to the CA-H900 heat-treated ones. This may be due to the longer duration of aging close to the austenite reversion temperature, and likely have resulted in partial reversion of the austenite. The reverted austenite then transforms to the martensite. The transformed-type texture components represent the texture formed from the parent austenite phase (face-centered cubic) during martensitic transformation.

Ping et al.[33] have shown the formation mechanism of lath martensite with a twin substructure with a {112}<111> relationship. Figure 6 shows the {112} pole figures as well as the linear misorientation profiles along the arrows elongated through the selected prior austenite grain (PAG) for the L-PBF and LP-DED specimens which have undergone CA-H900 and CA-H1150. The poles coincidence in the {112} maps for all the conditions are in line with the reported pole figures for martensite with the Kurdjumov–Sachs (K-S) relationship with the parent austenite.[34] In addition, the point-to-point misorientation profiles show the boundaries with 60° misorientation indicating the twin boundaries,[35] which further proves the twin-based martensitic transformation in the L-PBF and LP-DED 17-4 PH SS specimens.
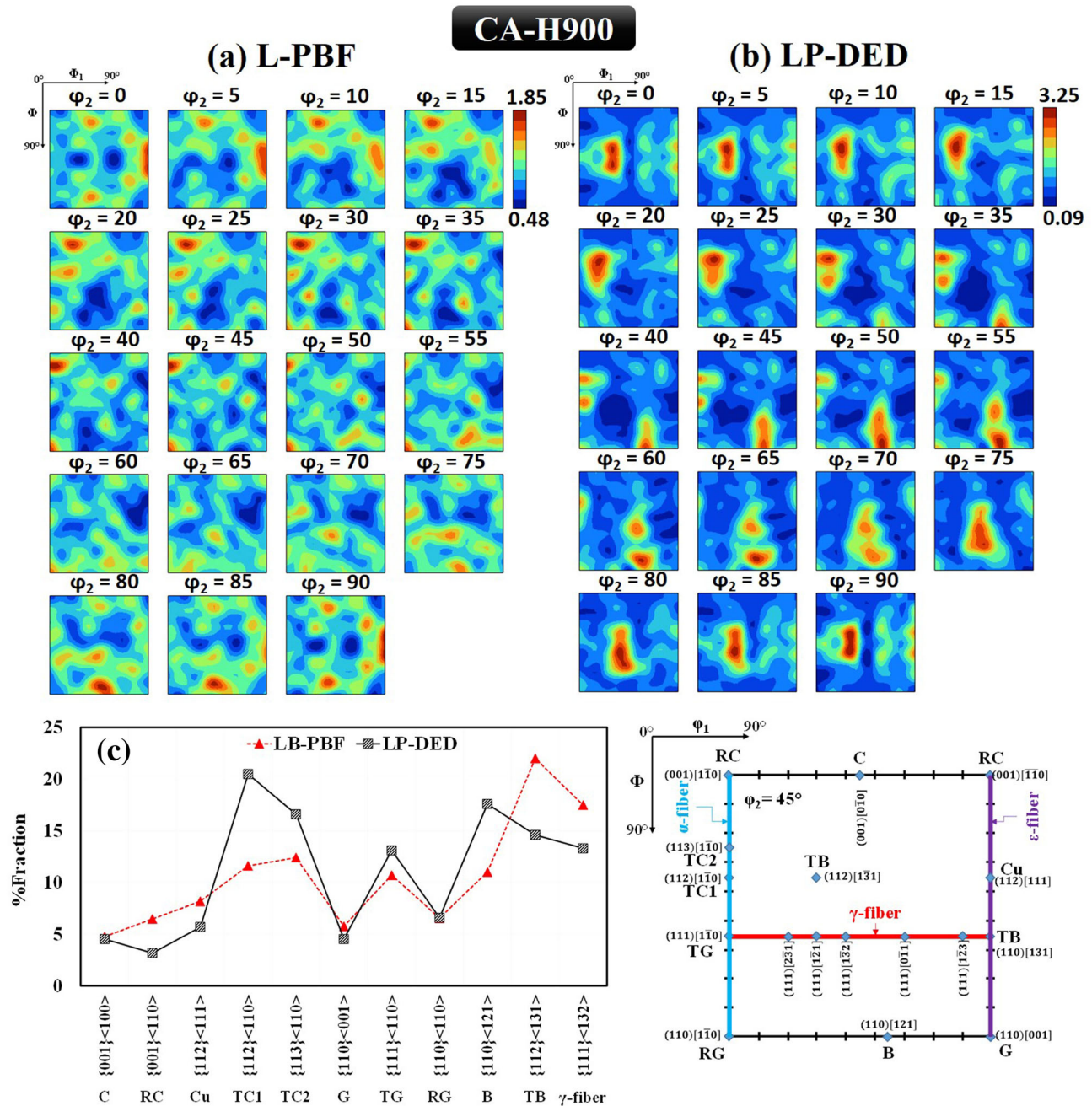
Fig. 4. ODF maps for the (a) L-PBF and (b) LP-DED 17-4 PH SS specimens, and (c) their quantified texture components for the CA-H900 heat treatment condition. A schematic of the important texture components in body-centered cubic for $\varphi_2 = 45°$ is also shown.

Tensile Behavior and Fractography Analysis

The engineering stress-engineering strain curves for the L-PBF and LP-DED specimens which have undergone CA-H900 and CA-H1150 heat treatment conditions are presented in Fig. 7a. The tensile properties (i.e., S_y, S_u, and %El) for the L-PBF, LP-DED, and wrought 17-4 PH SS are compared in Fig. 7b. In general, the peak-age heat treatment (i.e., CA-H900) results in the highest tensile strength in 17–4 PH SS at the expense of the ductility, whereas the over-aging heat treatment (i.e., CA-H1150) significantly reduces the strength and increases the ductility. The high tensile strength (i.e., S_y, S_u) after the CA-H900 condition is attributed to the formation of nano-sized Cu-enriched precipitates in this heat treatment condition, while these precipitates are coarsened upon over-aging resulting in higher ductility.[36]

Comparing the L-PBF and LP-DED specimens, the L-PBF specimens have higher tensile strength than those of the LP-DED counterparts regardless of the heat treatment condition. This is because of the finer microstructure obtained for the L-PBF
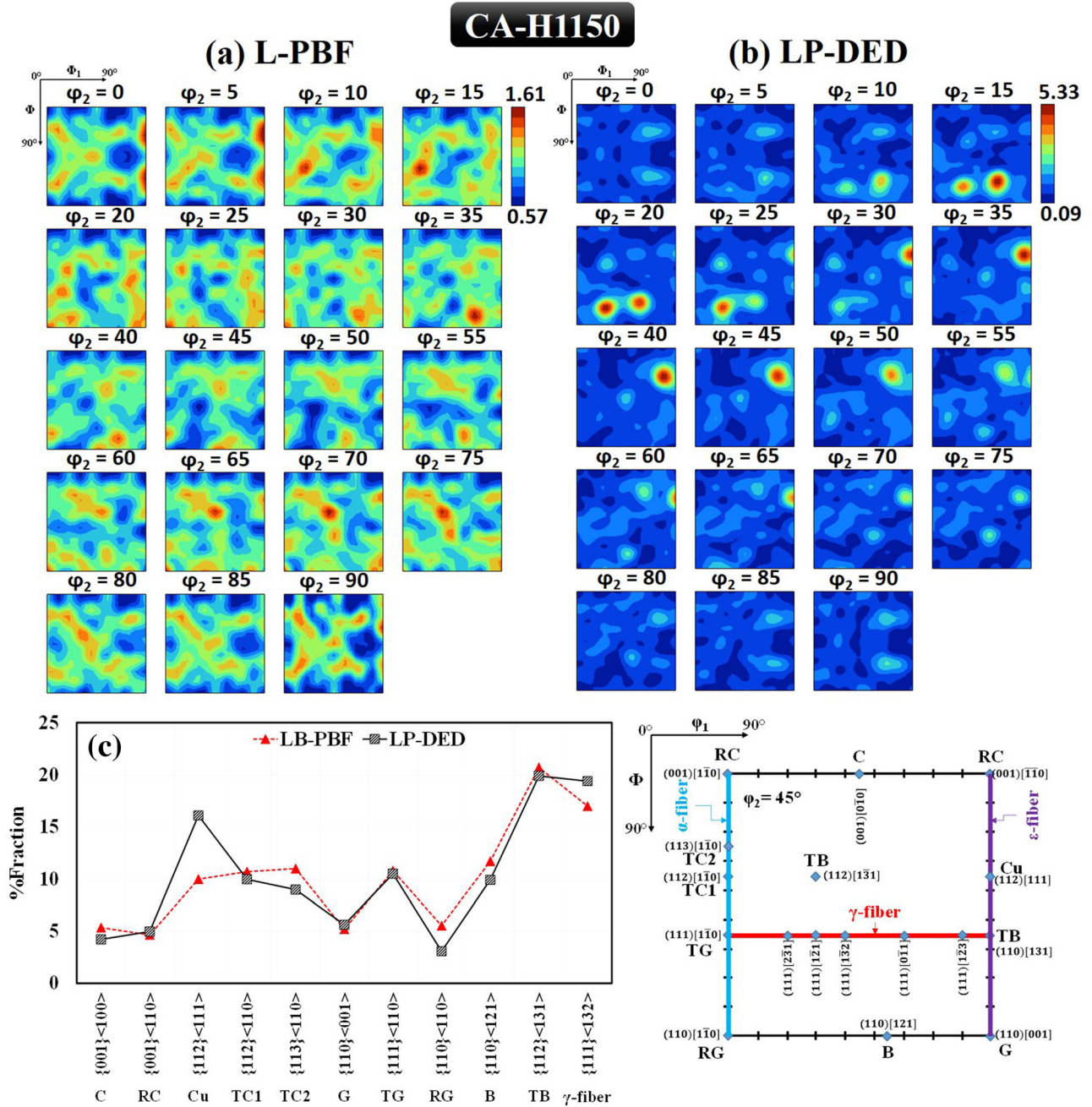
Fig. 5. ODF maps for the (a) L-PBF and (b) LP-DED 17-4 PH SS specimens, and (c) the quantified texture components for the CA-H1150 heat treatment condition. A schematic illustration of the important texture components in body-centered cubic for $\varphi_2 = 45°$ is also shown.

specimens compared with that of the LP-DED ones (see Fig. 3). The L-PBF specimen has higher tensile strength, whereas the LP-DED specimen possesses comparable tensile strength and ductility compared with the wrought 17-4 PH SS. The higher tensile properties of the L-PBF 17-4 PH SS are ascribed to its finer grain structure.

Although the CA-H900 heat treated LP-DED specimen has a lower tensile strength than the L-PBF counterpart and is expected to have higher ductility, its ductility is comparable to that of the L-PBF specimen with higher tensile strength. The loss

of the expected ductility in the CA-H900 heat-treated LP-DED specimen is due to the presence of δ-ferrite in its microstructure (see Fig. 3c). Figure 8 shows the kernel average misorientation (KAM), and the Schmid factor map of the body-centered cubic slip system (i.e., {110} <111>) along the loading direction (i.e., parallel to the Z axis) for the LP-DED 17-4 PH SS specimens heat treated at CA-H900 (Fig. 8a and b). The δ-ferrite phase is indicated by arrows in the KAM images and circled in the Schmid factor maps. As shown in Fig. 8a and b for the CA-H900 heat-treatment condition, the δ-
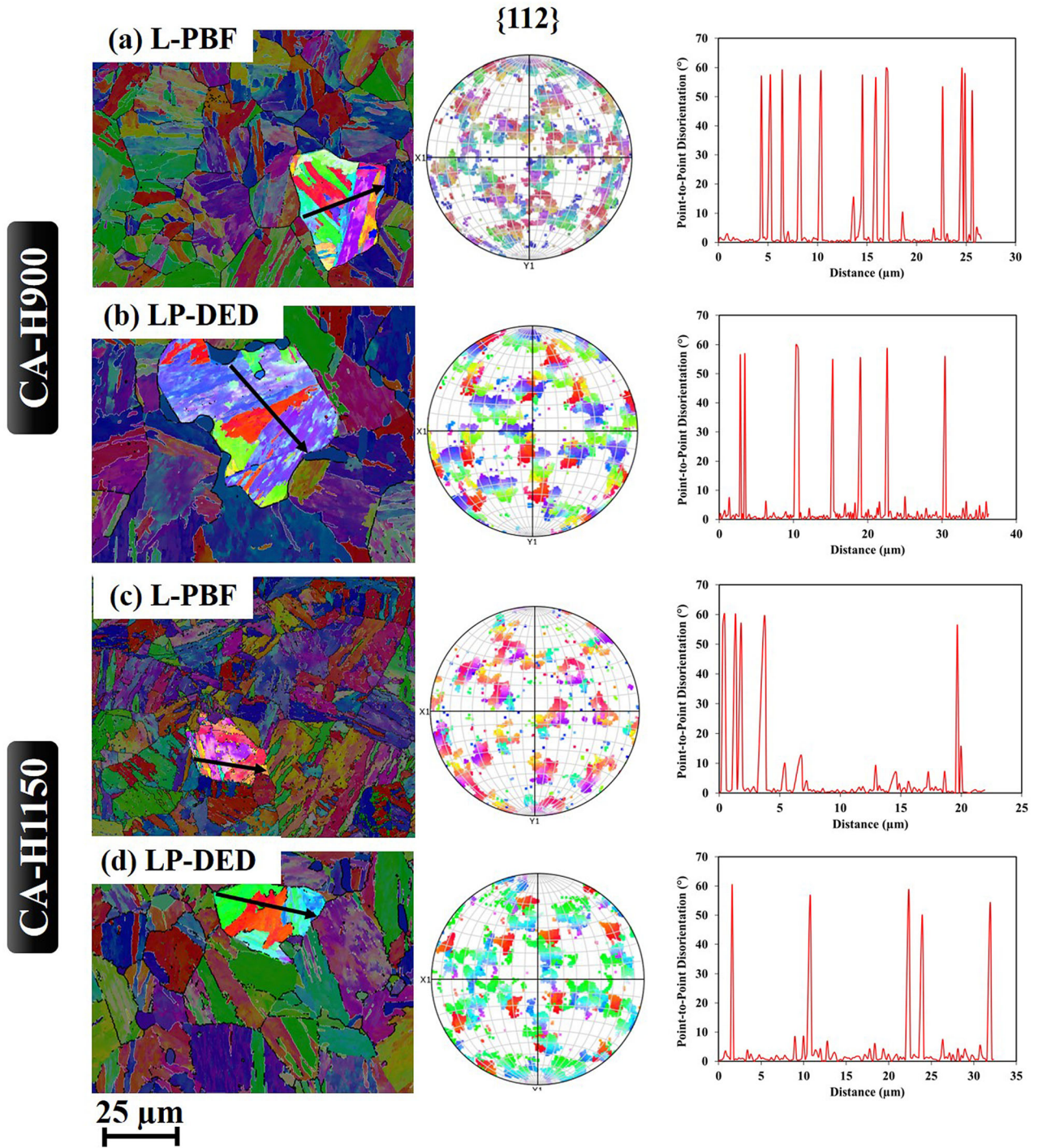
Fig. 6. IPF maps, {112} pole figures, and the point-to-point misorientation maps showing the twin-based substructure of the martensite in selected PAG of the L-PBF and LP-DED 17-4 PH SS specimens. CA-H900 condition: (a) L-PBF, (b) LP-DED, and CA-H1150 condition: (c) L-PBF, and (d) LP-DED.

ferrite phase not only has well-defined edges but it also has a strong contrast in the Schmid factor with the martensitic matrix; in other words, there is a high incompatibility between the δ-ferrite and the matrix resulting in loss of ductility considering that the material possesses high strength.

The fracture surfaces of the L-PBF and LP-DED 17-4 PH SS specimens are compared in Figure 9a for CA-H900 and Fig. 9b for the CA-H1150 heat-treatment conditions. Both conditions result in mostly axis-symmetric fracture surfaces with the shear lips of CA-H900 condition occupying very small area fractions and those of CA-H1150
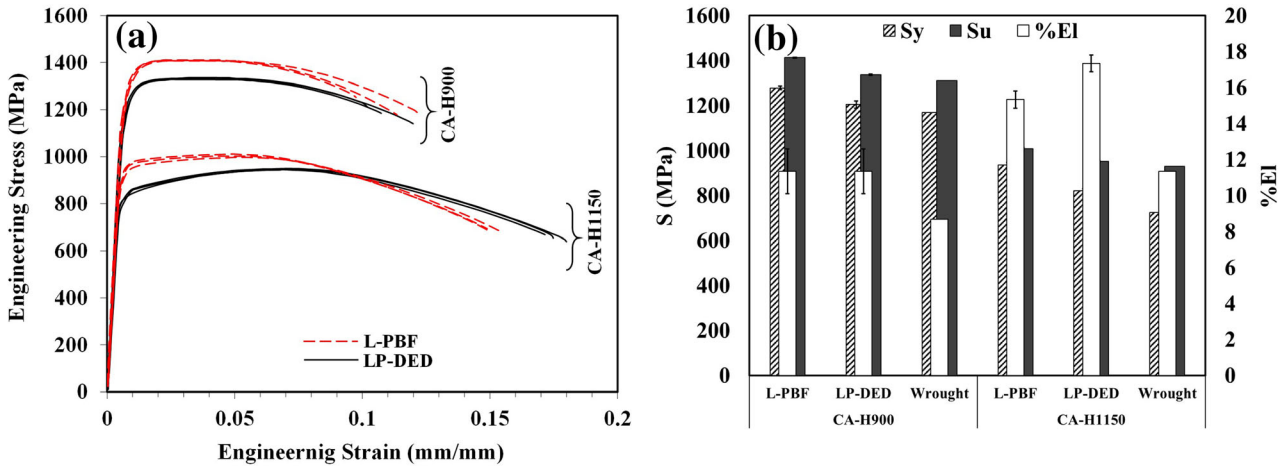
Fig. 7. Tensile behaviors of the L-PBF and LP-DED 17-4 PH SS specimens which have undergone CA-H900 and CA-H1150 heat treatment conditions: (a) flow stress curves, (b) summarized tensile properties, and (c) %elongation versus ultimate tensile strength. The wrought data has been. taken from ASTM A693[37]
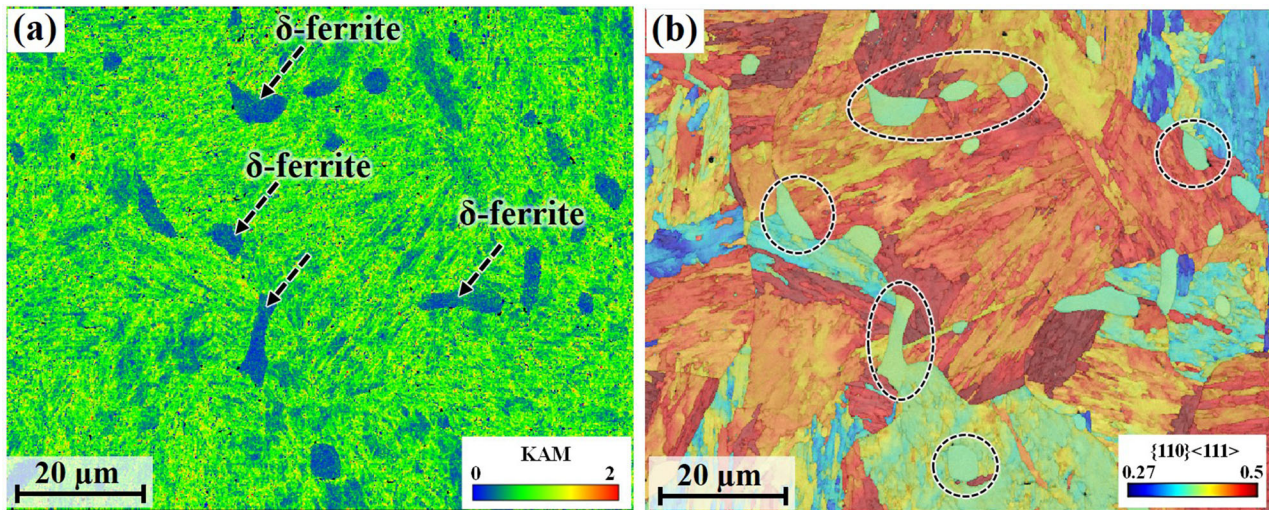

Fig. 8. Strain analysis of the δ-ferrite phase for the LP-DED 17-4 PH SS specimen which has undergone CA-H900 heat treatment condition: (a) KAM, (b) Schmid factor maps. Note the loading direction parallel to the Z-axis considered for generating the Schmid factor map.

condition being large. The very well-defined cup-and-cone feature CA-H1150 fracture surfaces (Fig. 9b) suggests that their fracture was very ductile. This is consistent with the presence of quasi-cleavage facets and cracks on the fracture surfaces of the CA-H900 heat treated specimens showing brittle behavior, while enormous dimples formed on the fracture surfaces of the CA-H1150 heat treated specimens representing ductile behavior.

Another main difference between the fracture surfaces of the L-PBF and LP-DED specimens is the presence of cracks in the CA-H900 condition, and dimples in the CA-H1150 condition. This suggests that the fracture surfaces of the former condition had radial zones which were evidence of rapid crack propagation, while the fractures of the latter condition were governed mainly by the nucleation, growth, and coalescence of voids as well as final

shearing.[38] The CA-H900-treated LP-DED specimen has larger cracks and facets than the L-PBF ones, which resulted in the loss of ductility despite of having lower strength. This may be related to the presence of large δ-ferrite in the microstructure of the LP-DED specimen, having high incompatibility with the matrix, which resulted in crack initiation and growth along the lath martensite boundaries. On the other hand, CA-H1150 treated LP-DED specimens have larger and deeper dimples due to the coarser microstructure, justifying its higher ductility compared with the L-PBF ones.

CONCLUSION

This study characterized and compared the non-heat treated (NHT) microstructures of 17–4 PH SS specimens fabricated via L-PBF and LP-DED AM processes. In addition, the effect of different heat-

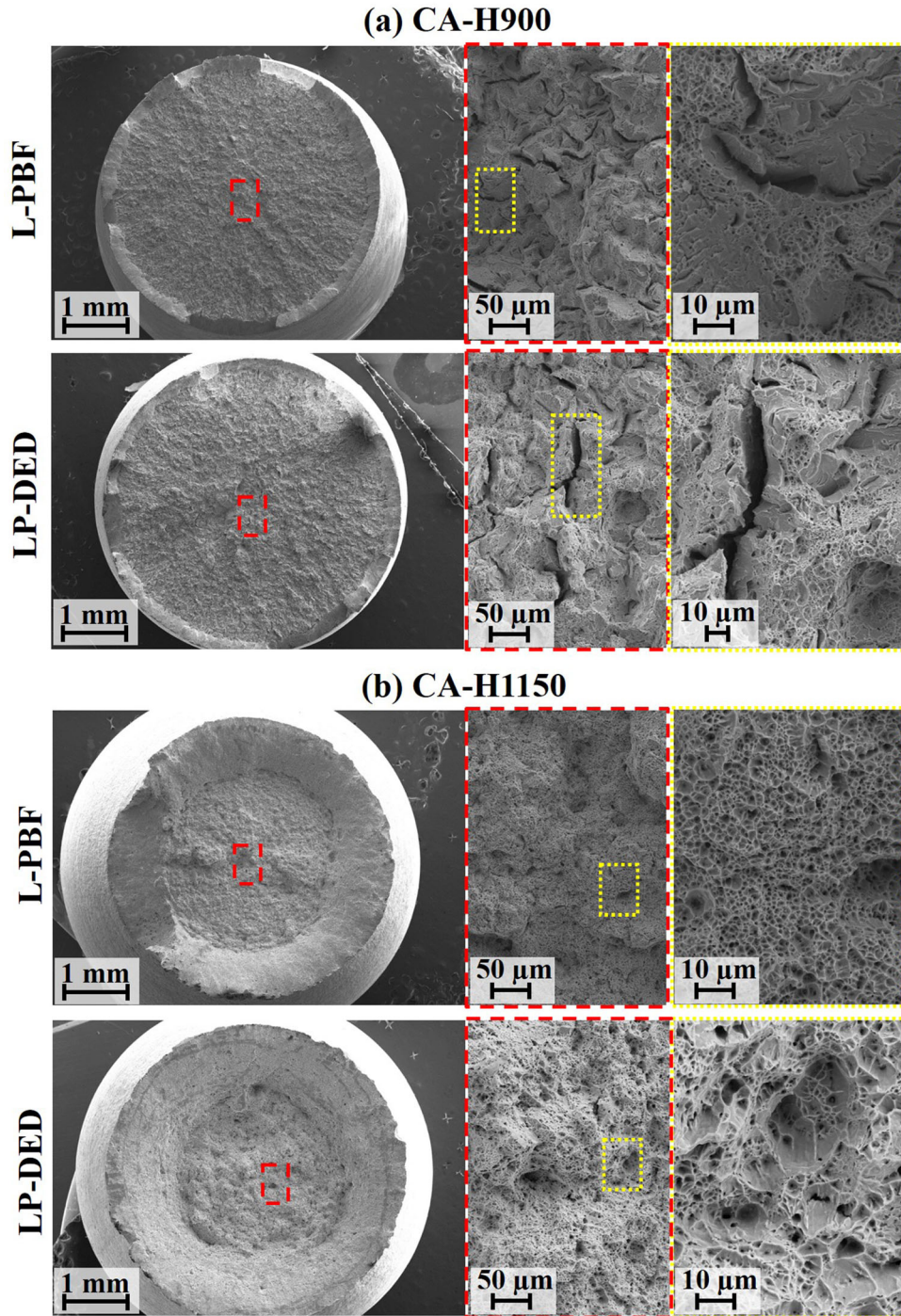## (a) CA-H900

(b) CA-H1150

Fig. 9. Tensile fracture surfaces of the L-PBF and LP-DED 17-4 PH SS specimens: (a) CA-H900, and (b) CA-H1150.

treatment procedures on the crystallographic texture and room-temperature tensile deformation behavior of L-PBF and LP-DED specimens were investigated. The following conclusions are drawn:

1. The NHT L-PBF 17–4 PH SS specimen had a more refined microstructure, constituted of equiaxed ferrite grains and lath martensite, whereas the microstructure of the LP-DED counterpart was composed of coarse massive

ferrite, with Widmanstätten ferrite grains decorating the grain boundaries. The variation in the cooling/solidification rates induced by the L-PBF and LP-DED processes and the differences in Cr_{eq}/Ni_{eq} values for the L-PBF and LP-DED specimens may have caused these differences in their NHT microstructures.

2. The δ-ferrite phase was retained in the microstructure of the LP-DED 17–4 PH SS

specimen at room temperature. This was ascribed to the lower cooling/solidification rate in the LP-DED process and higher Cr_{eq}/Ni_{eq} value of the LP-DED specimen compared to the L-PBF one, which stabilized ferrite in the microstructure.

3. The over-aging heat treatment procedure (i.e., CA-H1150) likely resulted in the reversion of austenite from martensite. However, the reverted austenite was retained in the microstructure of the L-PBF specimen, while it was transformed to martensite in the LP-DED counterpart upon cooling. The finer microstructure in the L-PBF specimen resulted in finer reverted austenite, which hindered the martensitic transformation.

4. A full heat treatment cycle is required for the L-PBF and LP-DED 17–4 PH SS specimens to diminish their variation in texture. Both the L-PBF and LP-DED specimens had a twin-based martensite with a K-S relationship to the parent austenite.

5. The L-PBF 17–4 PH SS specimen outperformed the LP-DED and wrought counterparts with the same heat treatment in the room-temperature tensile properties. This was attributed to the finer microstructure of the L-PBF specimens.

6. The δ-ferrite phase in the CA-H900 heat treated LP-DED specimen reduces the ductility compared with that of the L-PBF counterpart even though the LP-DED specimen had lower tensile strength. The high contrast between the Schmid factor of the δ-ferrite phase with the martensite matrix in the $\{110\} <111>$ slip system (i.e., high incompatibility with matrix), as well as the sharp edges of the δ-ferrite phase, justified the reduction in the ductility of the material.

7. The quasi-cleavage facets on the fracture surfaces of the CA-H900 treated specimens represented brittle behavior of the L-PBF and LP-DED 17–4 PH SS in the CA-H900 condition, while the fibrous fracture surface with dimples depicted ductile behavior of the material in CA-H1150 condition.

ACKNOWLEDGEMENTS

CONFLICT OF INTEREST

On behalf of all authors, the corresponding author states that there is no conflict of interest.

REFERENCES

1. N. Shamsaei, A. Yadollahi, L. Bian, and S.M. Thompson, *Addit. Manuf.* 8, 12 (2015).
2. D.D. Gu, W. Meiners, K. Wissenbach, and R. Poprawe, *Int. Mater. Rev.* 57, 133 (2013).
3. T.D. Ngo, A. Kashani, G. Imbalzano, K.T.Q. Nguyen, and D. Hui, *Compos. Part B* 143, 172 (2018).
4. T.F. Babuska, B.A. Krick, D.F. Susan, and A.B. Kustas, *Manuf. Lett.* 28, 30 (2021).
5. A. Jinoop, C. Paul, and K. Bindra, *J. Mater. Des. Appl.* 233, 2376 (2019).
6. R. Molaei, A. Fatemi, N. Sanaei, J. Pegues, N. Shamsaei, S. Shao, P. Li, D.H. Warner, and N. Phan, *Int. J. Fatigue* 132, 1 (2020).
7. J. Simpson, J. Haley, C. Cramer, O. Shafer, A. Elliott, B. Peter, L. Love, and R. Dehoff, ORNL/TM-2019-1190. *Oak Ridge Natl. Lab.* 1190, 1 (2019).
8. Q. Guo, C. Zhao, M. Qu, L. Xiong, L.I. Escano, S.M.H. Hojjatzadeh, N.D. Parab, K. Fezzaa, W. Everhart, T. Sun, and L. Chen, *Addit. Manuf.* 28, 600 (2019).
9. A. Saboori, A. Aversa, G. Marchese, S. Biamino, M. Lombardi, and P. Fino, *Appl. Sci.* 10, 3310 (2020).
10. M. Ma, Z. Wang, and X. Zeng, *Mater. Sci. Eng. A* 685, 265 (2017).
11. K.N. Amato, S.M. Gaytan, L.E. Murr, E. Martinez, P.W. Shindo, J. Hernandez, S. Collins, and F. Medina, *Acta Mater.* 60, 2229 (2012).
12. F. Liu, X. Lin, H. Leng, J. Cao, Q. Liu, C. Huang, and W. Huang, *Opt. Laser Technol.* 45, 330 (2013).
13. L.L. Parimi, G. Ravi, D. Clark, and M.M. Attallah, *Mater. Charact.* 89, 102 (2014).
14. W. Xu, M. Brandt, S. Sun, J. Elambasseril, Q. Liu, K. Latham, K. Xia, and M. Qian, *Acta Mater.* 85, 74 (2015).
15. B.E. Carroll, T.A. Palmer, and A.M. Beese, *Acta Mater.* 87, 309 (2015).
16. J. Schneider, *JOM* 72, 1085 (2020).
17. C. Doñate-Buendia, R. Streubel, P. Kürnsteiner, M.B. Wilms, F. Stern, J. Tenkamp, E. Bruder, S. Barcikowski, B. Gault, K. Durst, J.H. Schleifenbaum, F. Walther, and B. Gökce, *Procedia CIRP* 94, 41 (2020).
18. M.R. Stoudt, R.E. Ricker, E.A. Lass, and L.E. Levine, *JOM* 69, 506 (2017).
19. S. Cheruvathur, E.A. Lass, and C.E. Campbell, *JOM* 68, 930 (2015).
20. W. Liu, J. Ma, M.M. Atabaki, R. Pillai, B. Kumar, U. Vasudevan, H. Sreshta, and R. Kovacevic, *Lasers Manuf. Mater. Process* 2, 74 (2015).
21. S. Cao, *Determination of the Fe-Cr-Ni and Fe-Cr-Mo phase diagrams at intermediate temperatures using a novel dual-anneal diffusion-multiple approach*, Ph.D thesis, The Ohio State University, 2013.
22. TCFE9 Thermo-Calc Software, 1 (2017).
23. P.D. Nezhadfar, E. Burford, K. Anderson-Wedge, B. Zhang, S. Shao, S.R. Daniewicz, and N. Shamsaei, *Int. J. Fatigue* 123, 168 (2019).
24. P.D. Nezhadfar, P. Gradl, S. Shuai, and N. Shamsaei, In *Proc. 32nd Annu. Int. Solid Free. Fabr. Symp. – An Addit. Manuf. Conf.* (2021).
25. ASTM Standard E8/E8M-13a, *Standard Test Methods for Tension Testing of Metallic Materials* (2006).
26. T. LeBrun, T. Nakamoto, K. Horikawa, and H. Kobayashi, *Mater. Des.* 81, 44 (2015).
27. L. Facchini, N. Vicente, I. Lonardelli, E. Magalini, P. Robotti, and A. Molinari, *Adv. Eng. Mater.* 12, 184 (2010).
28. M. Alnajjar, F. Christien, K. Wolski, and C. Bosch, *Addit. Manuf.* 25, 187 (2019).
29. P.D. Nezhadfar, K. Anderson-Wedge, S.R. Daniewicz, N. Phan, S. Shao, and N. Shamsaei, *Addit. Manuf.* 36, 101604 (2020).
30. R.K. Okagawa, R.D. Dixon, and D.L. Olson, *Weld. Res. Suppl.* 62, 204s (1983).
31. P.D. Nezhadfar, R. Shrestha, N. Phan, and N. Shamsaei, *Int. J. Fatigue* 124, 188 (2019).

32. C. Celada-Casero, J. Sietsma, and M.J. Santofimia, *Mater. Des.* 167, 107625 (2019).
33. D.H. Ping, S.Q. Guo, M. Imura, X. Liu, T. Ohmura, M. Ohnuma, X. Lu, T. Abe, and H. Onodera, *Sci. Rep.* 8, 14264 (2018).
34. C. Cayron, *Acta Crystallogr. Sect. A* 69, 498 (2012).
35. P.D. Nezhadfar, A. Zarei-Hanzaki, S.S. Sohn, and H.R. Abedi, *Mater. Sci. Eng. A* 665, 10 (2016).
36. G.E. Dieter and D.J. Bacon, *Mechanical metallurgy* (McGraw-Hill, New York, 1986).
37. ASTM A693-16, *Standard specification for precipitation-hardening stainless and heat-resisting steel plate, sheet, and strip* (2016).
38. M.E. Stevenson, P.D. Umberger, and S.F. Uchneat, *Fracture appearance and mechanisms of deformation and fracture* (ASM International, 2021).